

**Physics-based network fine-tuning for robust quantitative susceptibility mapping
from high-pass filtered phase**

Jinwei Zhang^{1,2}, Alexey Dimov², Chao Li^{2,4}, Hang Zhang³, Thanh D. Nguyen²,
Pascal Spincemaille², Yi Wang^{1,2}

¹Meinig School of Biomedical Engineering, Cornell University, Ithaca, NY

²Department of Radiology, Weill Cornell Medicine, New York, NY

³Department of Electrical and Computer Engineering, Cornell University, Ithaca, NY

⁴Department of Applied Physics, Cornell University, Ithaca, NY

Correspondence:

Yi Wang, PhD.

Radiology, Weill Cornell Medicine

407 E 61st St, New York, NY 10065, USA

E-mail: yiwang@med.cornell.edu

Running title: SWI2QSM

Keywords: High-pass filtered phase, Quantitative Susceptibility Mapping, Physics-based neural network, Fine-tuning

Word count: ~2800

ABSTRACT

Purpose: To improve the generalization ability of convolutional neural network (CNN) based prediction of quantitative susceptibility mapping (QSM) from high-pass filtered phase (HPFP) image.

Methods: The proposed network addresses two common generalization issues that arise when using a pre-trained network to predict QSM from HPFP: a) data with unseen voxel sizes, and b) data with unknown high-pass filter parameters. A network fine-tuning step based on a high-pass filtering dipole convolution forward model is proposed to reduce the generalization error of the pre-trained network. A progressive Unet architecture is proposed to improve prediction accuracy without increasing fine-tuning computational cost.

Results: In retrospective studies using RMSE, PSNR, SSIM and HFEN as quality metrics, the performance of both Unet and progressive Unet was improved after physics-based fine-tuning at all voxel sizes and most high-pass filtering cutoff frequencies tested in the experiment. Progressive Unet slightly outperformed Unet both before and after fine-tuning. In a prospective study, image sharpness was improved after physics-based fine-tuning for both Unet and progressive Unet. Compared to Unet, progressive Unet had better agreement of regional susceptibility values with reference QSM.

Conclusion: The proposed method shows improved robustness compared to the pre-trained network without fine-tuning when the test dataset deviates from training. Our code is available at https://github.com/Jinwei1209/SWI_to_QSM/

INTRODUCTION

Susceptibility-weighted imaging (SWI) (1) is a widely used MRI method to visualize susceptibility sources, such as veins, calcifications and hemorrhages, by showing the effect of their tissue-induced magnetic field. SWI is obtained by combining the high-pass filtered phase (HPFP) and magnitude images of the gradient echo (GRE) data. The HPFP image is computed as the angle of the complex division of the original GRE by its low-pass filtered version. This operation suppresses the much larger background field which predominantly consists of low spatial frequency components and impedes clear visualization of the local tissue field (2). SWI has been used in clinical applications such as stroke, cerebrovascular disease and neurodegenerative disorders (3). However, this technique does not allow a direct quantitative measurement of the underlying tissue susceptibility.

Quantitative susceptibility mapping (QSM) (4) has been proposed to map tissue susceptibility by solving a dipole inversion problem. Typically, the tissue-induced field map is first obtained by fitting the phase of the complex multi-echo GRE data (5,6) followed by background field removal (7-10). Then, a regularized dipole inversion is performed to estimate the underlying tissue susceptibility distribution (11-14).

To date, a large amount of SWI HPFP data has been collected for which the underlying complex GRE data is no longer available. Despite potential interest in their quantitative analysis, accumulated HPFP images are incompatible with QSM reconstruction due to the removal of the low spatial frequency components of the tissue field, which is known to be a suboptimal method for the removal of background field as it removes some of the tissue field as well. Thanks to the rapid development of convolutional neural networks (CNNs) in medical imaging, there is an increasing interest in recovering QSM from HPFP data in SWI using CNNs (15-17). In one

approach, a 3D Unet (18,19) was applied to recover unfiltered phase data from HPFP data and compute QSM using the recovered phase data (16). A second approach reconstructs QSM directly from HPFP data, either using a network architecture with an edge prior and a cross dense block (15) or a generative adversarial network (GAN) (17). These promising results were obtained with the assumption that training and test data were acquired with the same imaging parameters. However, generalization errors may manifest when inference is attempted on data obtained by a different acquisition protocol, e.g., with different voxel size (15) and a different or unknown high-pass filter (16).

To address the issue of generalization errors of the pre-trained HPFP-to-QSM network, we propose to incorporate the forward model combining dipole convolution and high-pass filtering operations into the network for test-time fine-tuning (20,21). We also design a network architecture called “Progressive Unet” which consists of concatenating multiple Unets. During fine-tuning only the weights for the last Unet are updated for speeding up the inference step. Using a Progressive Unet, we observed an improved performance with similar computational cost for fine-tuning compared to the standard Unet implementation.

METHODS

Data acquisition and preprocessing

Data were acquired following an IRB approved protocol. All images used in this work were de-identified to protect the privacy of human participants.

Retrospective HPFP data

Multi-echo 3D GRE data acquired in 30 multiple sclerosis (MS) patients on a clinical 3T scanner (Siemens Healthineers) were retrospectively analyzed. The acquisition parameters were as follows: FA=15°, FOV = 24.0 cm, TE₁ = 6.3 ms, TR = 50.0 ms, #TE = 10, ΔTE = 4.1 ms, acquisition matrix = 320 × 320 × 48, voxel size = 0.75 × 0.75 × 3 mm³. The tissue field was estimated using non-linear fitting of the multi-echo phase data (6), followed by phase unwrapping and background field removal (7). QSM was reconstructed using Morphology Enabled Dipole Inversion (MEDI) (11). The HPFP f_{HPF} at TE₄ = 22.7 ms was computed retrospectively as the phase of the original complex image of slice c divided by its Hann low-pass filtering $H_{FC}(\cdot)$:

$$f_{HPF} = \angle \left(\frac{c}{H_{FC}(c)} \right), \quad (1)$$

18/2/10 of 30 patients were used as training/validation/test datasets. 3D patches with patch size 128*128*32 and extraction step size 90*90*10 were extracted for training and validation. Whole 3D volumes were fed into the network for testing.

Prospective HPFP data

3D GRE data was acquired prospectively in 9 healthy volunteers with both single-echo (TE = 22.7 ms, TR = 50.0 ms) and multi-echo acquisitions using the same 3T Siemens scanner and imaging parameters identical to the retrospective HFPP dataset. HPFP and SWI images from

the single-echo GRE data were generated prospectively by the scanner software with unknown high-pass filter parameters. QSM was reconstructed from the multi-echo GRE data using the same pipeline as the retrospective HPFP dataset. This formed another test set with prospective HPFP inputs and the corresponding QSM references.

Network pre-training and fine-tuning

Network pre-training

Inspired by (22), a progressive 3D Unet architecture with sequentially concatenated $K = 4$ Unets was constructed to predict QSM from HPFP (Figure 1). N^{th} Unet predicted an intermediate QSM_n from the input consisting of QSM_{n-1} generated by preceding Unet unit and the original HPFP. The purpose of such architecture was to progressively refine the network prediction in an iterative way, mimicking the numerical optimization scheme with iterative update of target solution. In the progressive Unet, a sum of L_1 losses between the output of each Unet and the QSM label was used to train the network with Adam optimizer (23) with learning rate $1e-3$ and 100 epochs on an RTX2080Ti GPU. In 3D Unet, each convolutional layer consisted of 3D convolution, batch normalization (24) and ReLU activation operations. Four levels of down-sampling with 32, 64, 128, and 256 output channels were used in 3D Unet to extract multiscale features.

Physics-based FINE-tuning

During testing, the last Unet in the pre-trained network was fine-tuned using the following high-pass filtering dipole convolution forward model on the whole 3D volume:

$$loss_{FT} = \left\| \angle \left(\frac{m \cdot e^{i(d*x)}}{H_{FC}(m \cdot e^{i(d*x)})} \right) - f_{HPF} \right\|_2^2, \quad (2)$$

where m is the magnitude image at the corresponding SWI echo time, d is the dipole kernel, x is the QSM output of the last Unet with fixed input HPFP f_{HPF} and QSM from the preceding Unet. As a result, f_{HPF} is used in both network input and fine-tuning loss function in a self-supervised fashion. During fine-tuning, the relative cutoff frequency FC in $H_{FC}(\cdot)$ was selected as 1/2 of the largest in-plane matrix dimension (320). The loss function in Eq. 2 was backpropagated until the input of the last Unet to update the pre-trained weights of the last Unet alone. Adam optimizer with 1e-4 learning rate was used and fine-tuning was terminated when the relative change of $loss_{FT}$ in Eq. 2 between two consecutive iterations fell below 5×10^{-3} (21) or started to fluctuate. Because the network weights of the last Unet are updated specifically for the test data in question, network inference has an increased computational cost of 12.0 seconds per case on average compared to a single pass through the network with fixed weights, which requires 1.0 second per case on average. As a comparison, the time required for single pass and fine-tuning of a vanilla Unet is 0.6 seconds and 12.0 seconds per case on average, respectively.

Experiments

Retrospective HPFP dataset with various FC s

To test how physics-based fine-tuning can improve the generalization ability of the pre-trained network to unknown Hann filters not seen during training, HPFP test data with various FC s (1/4, 3/8, 1/2, 5/8 and 3/4) in the Hann filters was calculated. The same QSM labels were used to compute network prediction accuracy. During fine-tuning, FC in Eq. 2 was fixed as 1/2 when tested on HPFP test data generated with any FC , simulating practical situation of a priori unknown cutoff frequency.

Retrospective HPFP dataset with various voxel sizes

To test the generalization ability to voxel sizes not seen during training, multi-echo complex GRE data with the original in-plane voxel size $0.75 \times 0.75 \text{ mm}^2$ (matrix size: 320×320) was resampled to in plane voxel sizes $0.577 \times 0.577 \text{ mm}^2$, $0.938 \times 0.938 \text{ mm}^2$, and $1.25 \times 1.25 \text{ mm}^2$ (matrix sizes 416×416 , 256×256 , and 192×192 , respectively), while slice thickness was kept the same. Resampling was implemented as k-space zero-padding or truncation of the original complex data. QSM labels for each voxel size were computed from the resampled data following the same processing pipeline as the original data. During fine-tuning, voxel size used in the dipole kernel d in Eq. 2 was modified accordingly.

Prospective HPFP dataset

To test the generalization ability of the proposed physics-based fine-tuning to unknown high-pass filtering process, HPFP and magnitude images computed by the scanner software from the single-echo GRE data were used in the fine-tuning loss Eq. 2 and the same HPFP image was also fed into the network as input. The relative cut-off frequency FC in Eq. 2 was fixed to $1/2$. QSM from the multi-echo GRE data was used as reference for comparison.

Performance comparison

The proposed progressive Unet with physics-based fine-tuning (Prognet-FT) was compared to the pre-trained progressive Unet (Prognet), pre-trained Unet (Unet) and Unet with physics-based fine-tuning (Unet-FT). For both retrospective HPFP datasets, root mean squared error (RMSE), peak signal-to-noise ratio (PSNR), structure similarity index (SSIM) and high-frequency error norm (HFEN) metrics were used to quantify the QSM reconstruction accuracy (25). For the prospective HPFP dataset, regions of interest (ROIs) in the left and right caudate

nuclei (CN), globus pallidus (GP) and putamen (PU) were manually segmented and mean susceptibility values of these ROIs were computed and compared.

RESULTS

Figure 2a shows the predicted QSMs of one retrospective HPFP test case with cutoff frequency $FC = 3/8$, where Unet and Prognnet reconstructions suffered from moderate blurring and GP over-estimation (red arrows), but both issues were mitigated by Unet-FT and Prognnet-FT. Figure S1 shows the predicted QSMs with $FCs = 1/4, 3/8, 1/2, 5/8$ and $3/4$. At $FC = 1/2$ (i.e., FC used for training), a visible over-estimation of GP was observed in Unet reconstruction but was reduced in Unet-FT, Prognnet and Prognnet-FT reconstructions (red arrows). At $FC = 5/8$ and $3/4$, GP over-estimation was also observed in Unet but was reduced in Unet-FT (red arrows). Slight under-estimation of GP was observed in Prognnet and Prognnet-FT (red arrows). At $FC = 1/4$, all methods suffered from large performance degradation with excessive image blurring where fine-tuning was not able to improve the image quality.

Figure 2b shows the boxplot of quantitative metrics across 10 test subjects with different FCs . At $FC = 3/8, 1/2, 5/8$ and $3/4$, the reconstruction accuracy of Unet and Prognnet was consistently improved in Unet-FT and Prognnet-FT with physics-based fine-tuning. Prognnet slightly outperformed Unet both before and after fine-tuning. At $FC = 1/4$, the reconstruction accuracy of Unet and Prognnet was dramatically decreased compared to the other FCs and fine-tuning resulted in worse accuracy.

Figure 3a shows the predicted QSMs of one retrospective HPFP test case with isotropic in-plane voxel size = 1.25mm, where GP over-estimation (red arrows) and image blurriness were observed in Unet and Prognnet, but were reduced in Unet-FT and Prognnet-FT. Figure S2 shows the predicted QSMs with voxel sizes = 0.577, 0.75, 0.938 and 1.25 mm. At voxel size = 0.75 mm voxel size (i.e., voxel size used for training), a visible over-estimation of GP was observed in Unet reconstruction but was reduced in Unet-FT, Prognnet and Prognnet-FT reconstructions (red

arrows). At voxel size = 0.938 and 1.25 mm, besides GP over-estimation in Unet reconstruction, increased image blurring was also observed with increased voxel size, while Unet-FT managed to reduce the blurriness and GP over-estimation. Prognnet reconstruction was less blurry than Unet and was improved in Prognnet-FT. At voxel size = 0.577 mm, slight blurriness was observed in Unet and Prognnet and was reduced associated with application of fine-tuning.

Figure 3b shows the boxplot of quantitative metrics across 10 test subjects with different in-plane voxel sizes. Reconstructions of Unet and Prognnet were consistently improved after physics-based fine-tuning at all voxel sizes tested in the experiment. Prognnet slightly outperformed Unet both before and after fine-tuning at all voxel sizes.

Figure 4a shows the predicted QSMs of two prospective HPFP test cases. For both cases, Unet and Prognnet visually appeared blurry compared to the reference QSMs. The blurring was suppressed after fine-tuning in Unet-FT and Prognnet-FT. Figure 4b shows the comparison of average ROI values across 9 test subjects. Unet and Unet-FT had under-estimation in CN and GP, while Prognnet and Prognnet-FT had slight under-estimation in CN.

DISCUSSION

In the present work, we proposed a physics-based network fine-tuning method to improve the generalization ability of reconstructing QSM from HPFP data using deep learning.

Experiments in both retrospective and prospective in vivo data demonstrate improved QSM reconstruction accuracy after fine-tuning when test dataset imaging and postprocessing parameters deviate from those encountered during training.

The major contribution of our work is the utilization of the forward physical model or fidelity loss for test time fine-tuning to reduce generalization errors of deep learning. Such fidelity imposed network edit (FINE) approach was proposed in prior work (21) for ill-posed dipole inversion using deep learning (26-31), and has been applied to related inverse problems such as water-fat separation (32). Compared to dipole inversion, QSM reconstruction from HPFP data is a more ill-posed inverse problem, due to properties of both the dipole kernel and the inherent incompleteness of the input data (Eq. 2). Unets have been used to map the filtered tissue field into QSM (15-17). However, depending on the training data, these networks may not properly reconstruct features not encountered in the training dataset, such as different voxel sizes (Figure 2), or when the test data was generated with unknown filter parameters (Figures 3 and 4). The proposed fine-tuning step is designed to reduce generalization errors due to such domain shifts and overcome network's lack of fidelity in the test data.

In the present work we show that network fine-tuning results in improved accuracy of QSM reconstruction from HPFP data under small-to-moderate deviations of filter parameters relative to the training data ($FC = 3/8$ and $5/8$ in Figure S1). A possible explanation for this insensitivity is that high-pass filter parameters typically selected in practical setting impose very aggressive filtering, preserving only sparse details such as phase edges. Therefore, the exact

detail of the low frequency suppression may be less important, leading to a low inconsistency between measured HPFP data and data predicted by a possibly inaccurate forward model. However, such explanation does not hold with more information filtered out ($FC = 1/4$ in Figure S1), where under such a large test case deviation, excessive blurring in Unet and Prognnet reconstructions was even exaggerated by fine-tuning, leading to worse reconstruction accuracy.

Another advantage of the proposed approach is the progressive network architecture integrating the advantages of deep learning feature extraction and classical optimization iterative scheme. To this end, the identical Unet blocks were stacked successively to mimic the iterative steps of optimization algorithms (22). By combining a few refining modules, the quality of the susceptibility distribution image derived from the incomplete HPFP data might be progressively improved through module iterations. Additionally, in terms of network fine-tuning, progressive Unet architecture does not increase the computational cost of the physics-based fine-tuning compared to Unet-FT as only the last Unet is updated during test time. Our results suggest that such progressive architecture yields higher reconstruction accuracy compared to Unet in both pre-trained and fine-tuned networks (Figures 2b and 3b).

There are several limitations present in this work. First, the effectiveness of the progressive architecture needs to be assessed with respect to the number of repeating units. Second, the computational cost of fine-tuning (12.0 seconds per case on average) is higher than a single pass (1.0 second per case on average) through a deep neural network due to the additional network update based on the iterative optimization. Efficiency of fine-tuning also requires further analysis. Third, unrolled architecture needs to be investigated as another strategy incorporating physical model into deep learning. Unrolled network architectures have become popular in QSM-related research, with applications in multi-echo gradient echo sequence

acceleration (31,33,34) and dipole inversion (35-37). Unrolled networks are inspired by classical optimization schemes replacing hand-crafted regularizations with deep learning modules (38).

As a result, unrolled networks leverage both the advantages of forward physical model incorporation and progressive architecture. Future work should also include implementation of the unrolled architecture for QSM reconstruction from HFPF data.

CONCLUSION

In summary, the physics-based fine-tuning strategy is useful for solving ill-posed high-pass filtered dipole inversion inverse problem and reduces generalization errors of end-to-end neural networks.

FIGURES

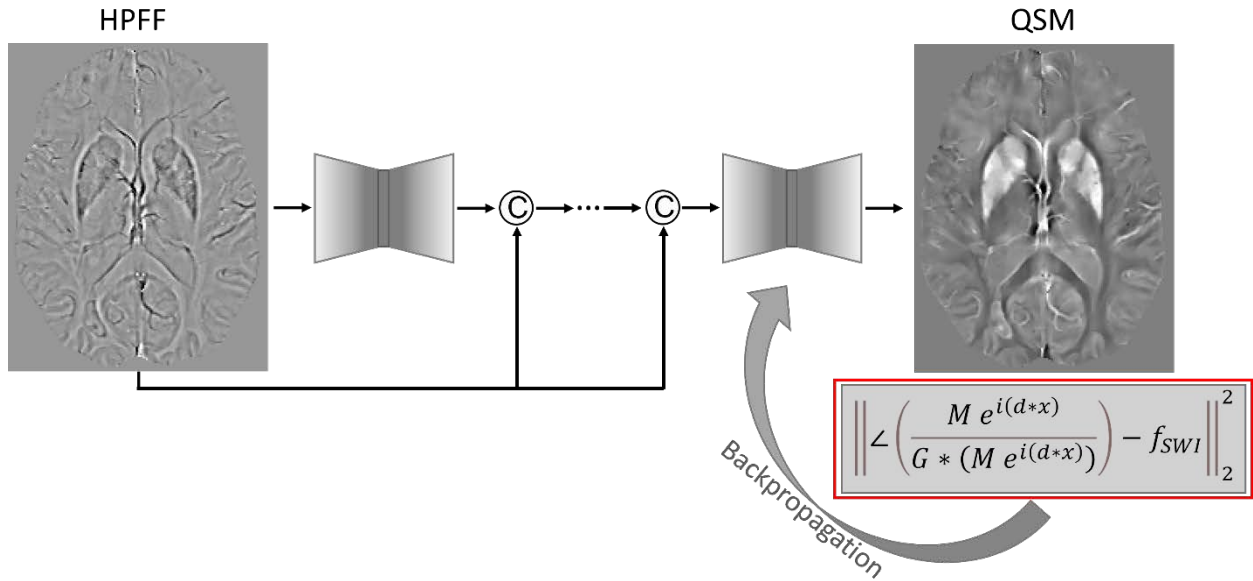


Figure 1. Proposed progressive 3D Unet architecture and its fine-tuning using high-pass filtering dipole convolution forward model. QSM prediction is progressively refined after each Unet during forward pass. Fine-tuning backpropagation is deployed only in the last Unet to save computational cost.

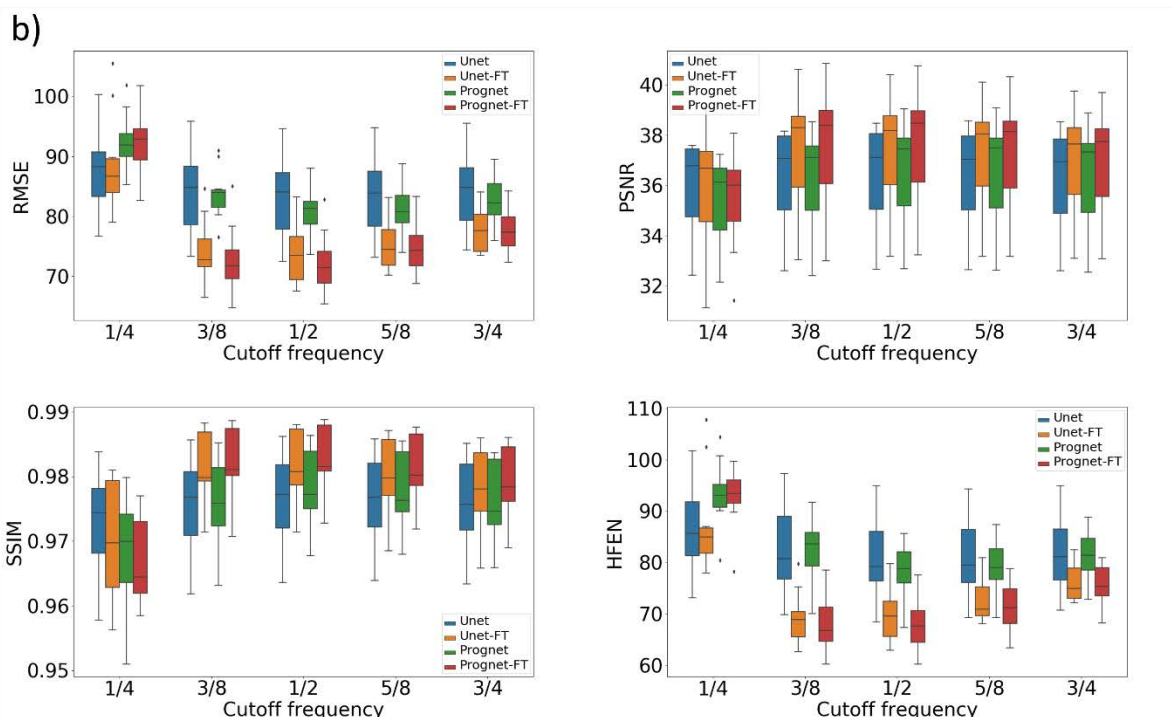
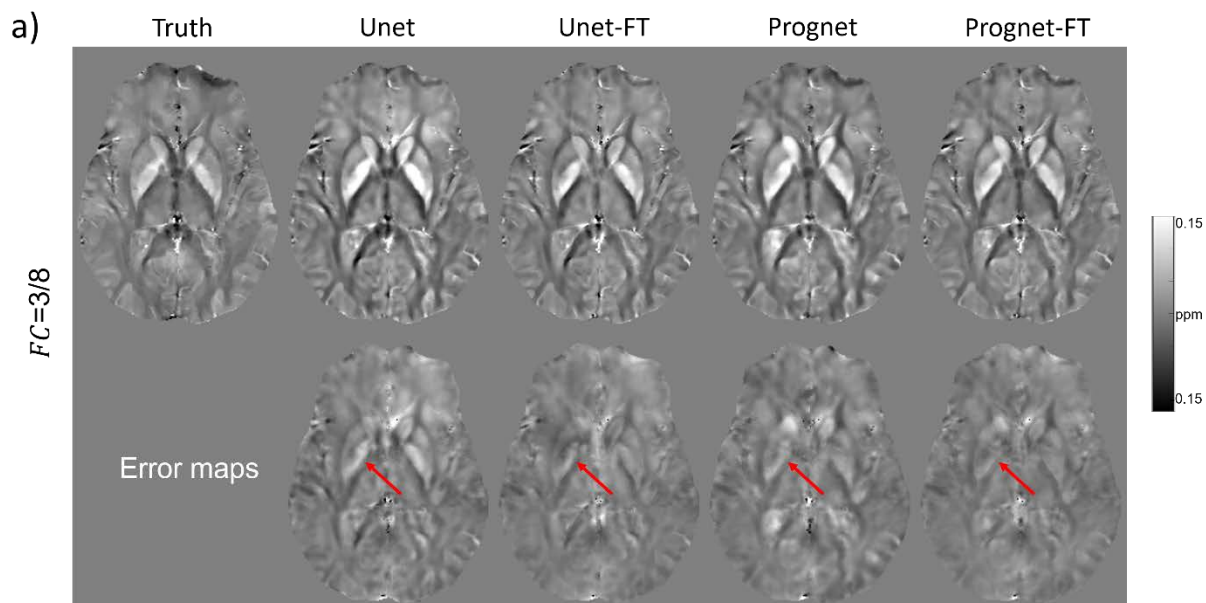


Figure 2. (a) Retrospective HPFP test case with cutoff frequency $FC = 3/8$ in Hann filters. $FC = 1/2$ was used in the training dataset as well as fine-tuning loss function Eq. 2. Moderate image blurring and GP over-estimation in Unet and Prognet reconstructions were mitigated by Unet-FT and Prognet-FT (red arrows). Test results with $FCs = 1/4, 3/8, 1/2, 5/8$ and $3/4$ in Hann filters are

shown in Supplementary Figure S1. (b) Quantitative comparison of reconstruction methods with $FCs = 1/4, 3/8, 1/2, 5/8$ and $3/4$ in test data Hann filters. At $FC = 3/8, 1/2, 5/8$ and $3/4$, the reconstruction accuracy of Unet and Prognnet was improved in Unet-FT and Prognnet-FT. Prognnet slightly outperformed Unet both before and after fine-tuning. At $FC = 1/4$, all methods suffered from performance degradation and fine-tuning resulted in worse accuracy.

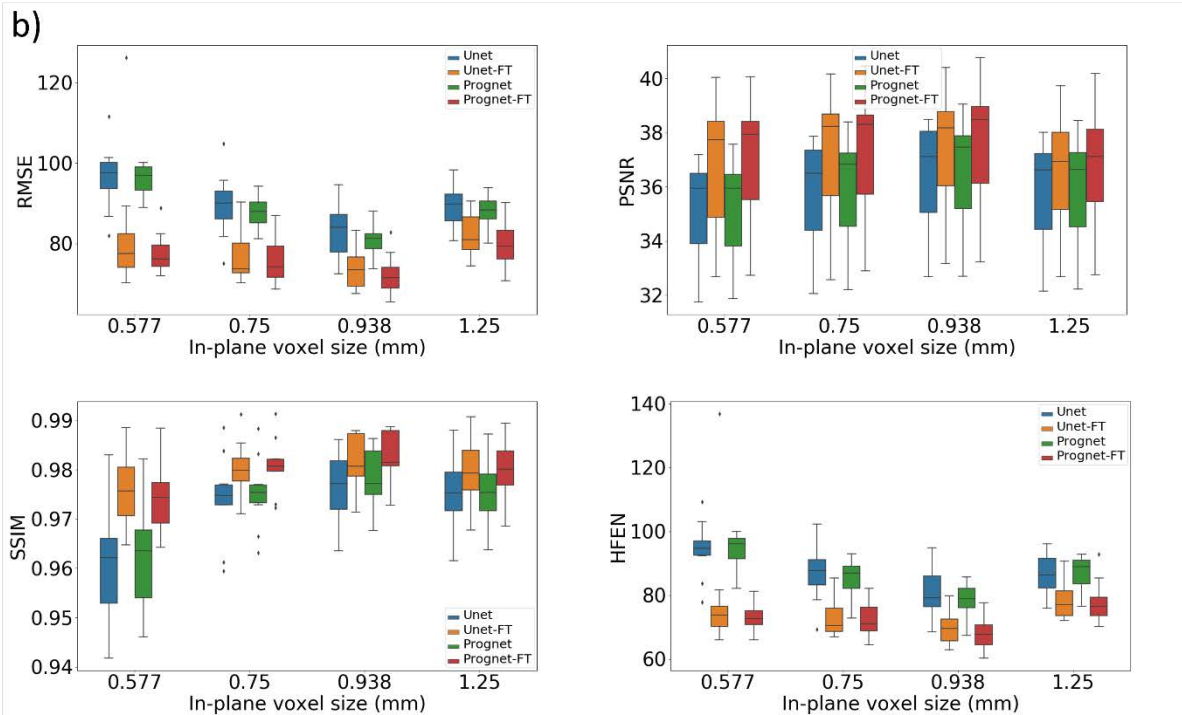
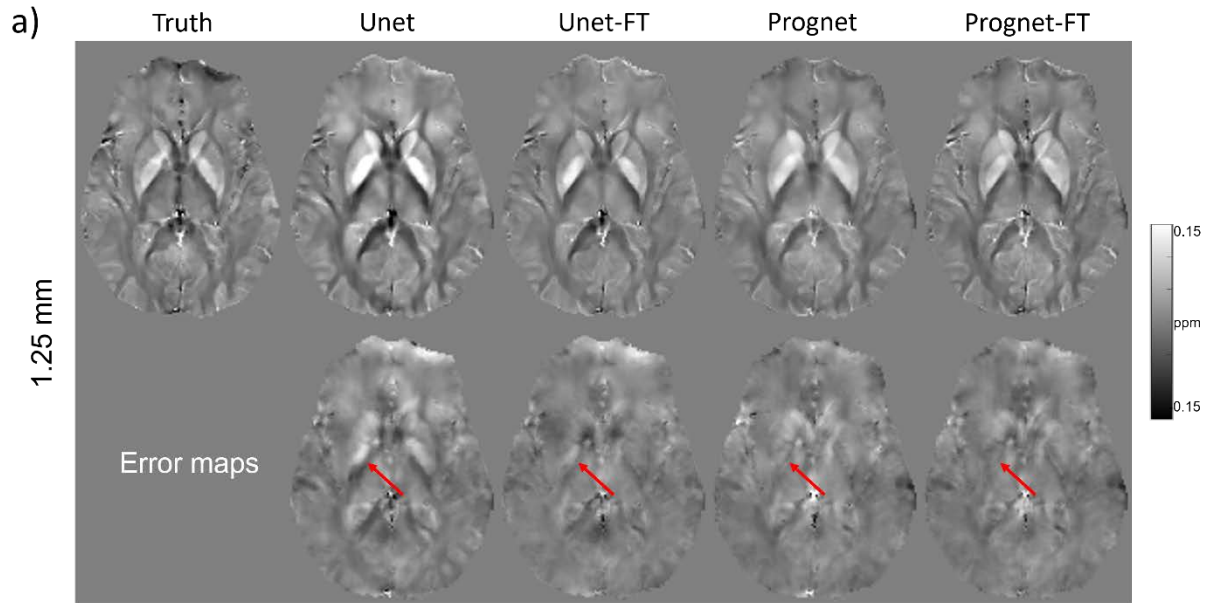


Figure 3. (a) Retrospective HPFP test case with isotropic in-plane voxel size = 1.25 mm. Voxel size = 0.75 mm was used for training. Both GP over-estimation (red arrows) and image blurriness were observed in Unet and Prognet as the test case voxel size increased, but were reduced in Unet-FT and Prognet-FT. Prognet reconstruction was less blurry than Unet. (b)

Quantitative comparison of reconstruction methods with isotropic in-plane voxel sizes = 0.577, 0.750, 0.938 and 1.25 mm. At all voxel sizes, the reconstruction accuracy of Unet and Prognnet was improved in Unet-FT and Prognnet-FT. Prognnet slightly outperformed Unet both before and after fine-tuning.

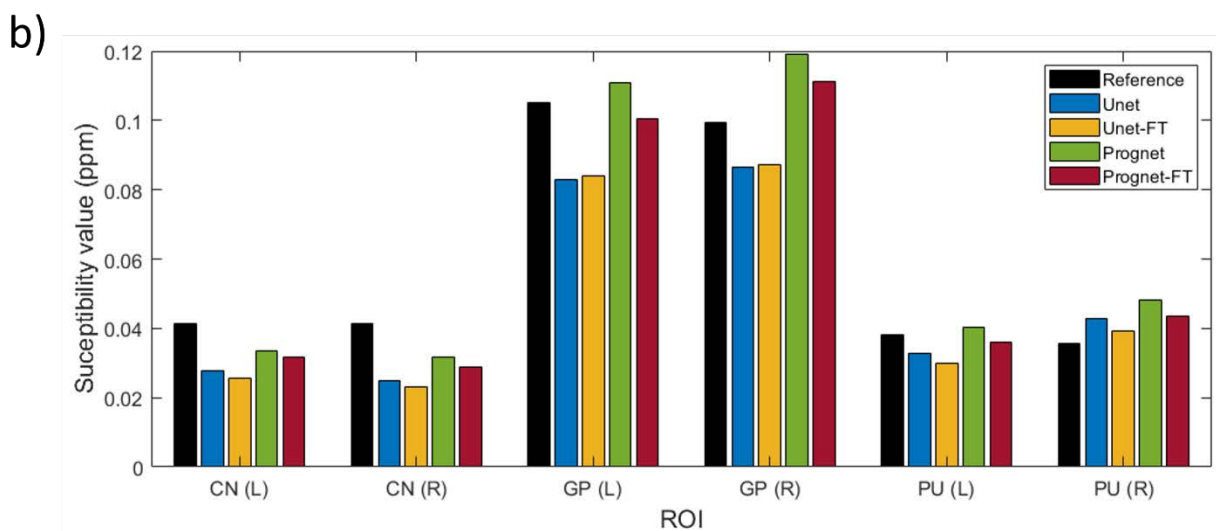
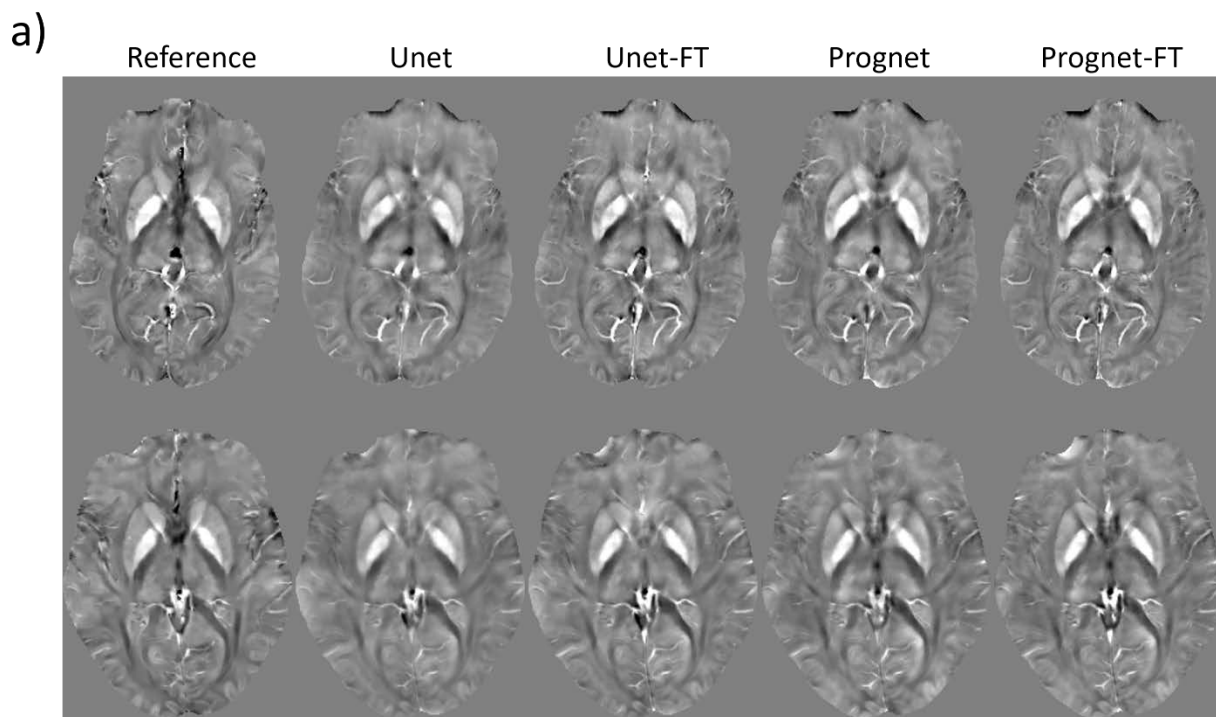


Figure 4. (a) Predicted QSMs of two prospective HPFP test cases and (b) ROIs analysis averaged over 9 test cases. In (a), compared to the reference QSMs, blurriness for both cases in Unet and Prognet was reduced after fine-tuning in Unet-FT and Prognet-FT. In (b), all four methods had slight under-estimation in CN. Unet and Unet-FT had additional under-estimation in GP.

SUPPLEMENTARY FIGURES

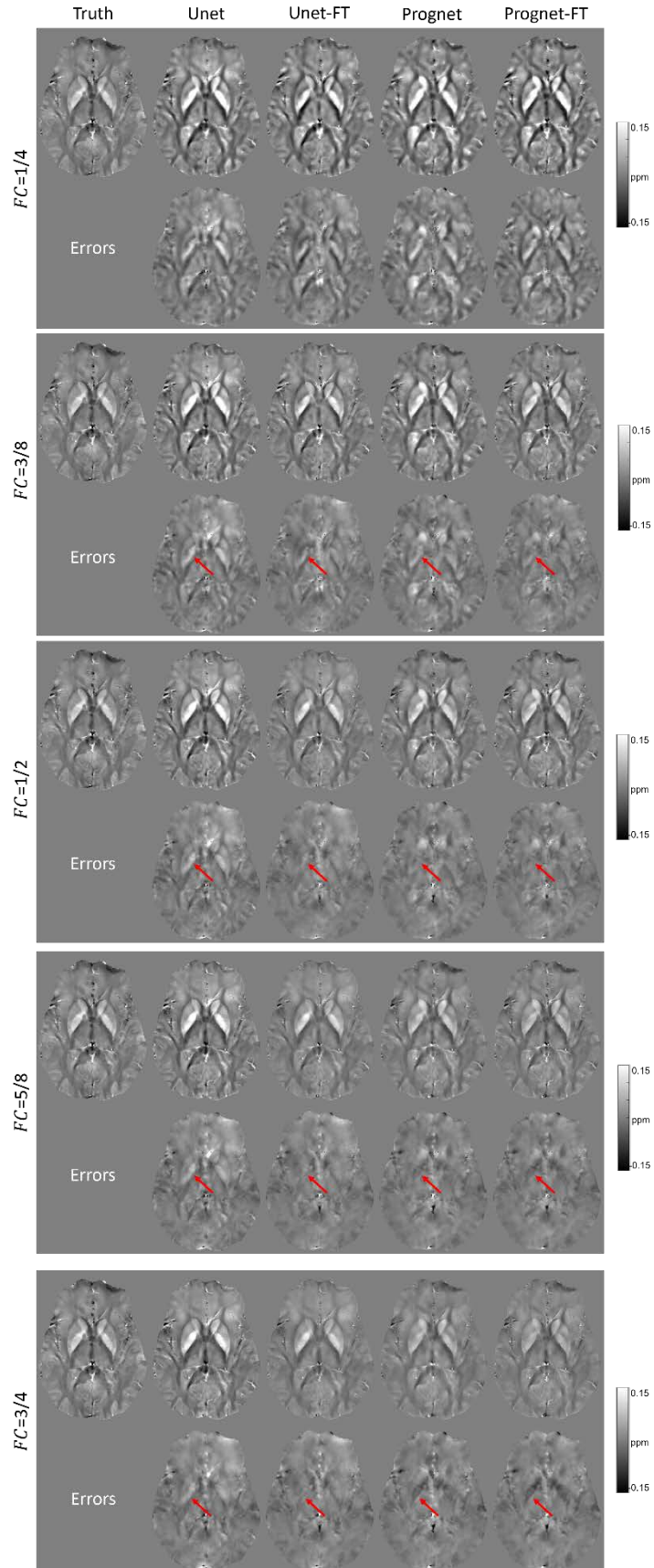


Figure S1. Retrospective HPFP test case with cutoff frequency FCs = $1/4$, $3/8$, $1/2$, $5/8$ and $3/4$ in Hann filters. FC = $1/2$ was used in the training dataset as well as fine-tuning loss function Eq. 2. At FC = $1/2$, visible over-estimation of GP in Unet reconstruction was reduced in Unet-FT, Prognnet and Prognnet-FT reconstructions (red arrows). At FC = $3/8$, moderate image blurring and GP over-estimation in Unet and Prognnet reconstructions were mitigated by Unet-FT and Prognnet-FT (red arrows). At FC = $5/8$ and $3/4$, GP over-estimation in Unet was reduced in Unet-FT (red arrows). Slight under-estimation of GP was observed in Prognnet and Prognnet-FT (red arrows). At FC = $1/4$, excessive image blurring was observed in Unet, Unet-FT, Prognnet and Prognnet-FT reconstructions.

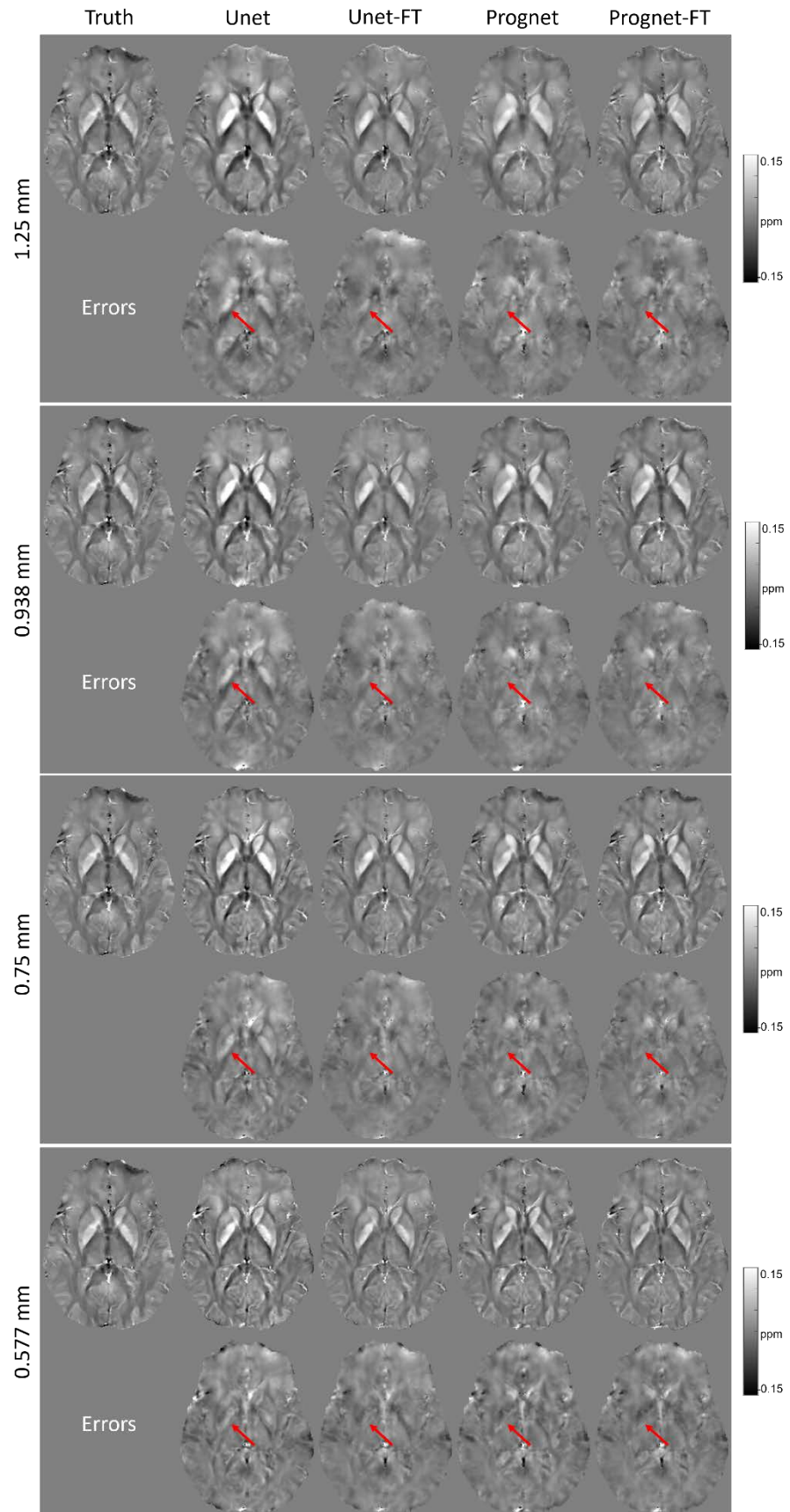


Figure S2. Retrospective HPFP test case with isotropic in-plane voxel sizes = 0.577, 0.75, 0.938 and 1.25 mm. Voxel size = 0.75 mm was used for training. At voxel size = 0.75 mm, visible over-estimation of GP in Unet reconstruction was reduced in Unet-FT, Prognnet and Prognnet-FT reconstructions (red arrows). Besides GP over-estimation, increased image blurring were observed in Unet and Prognnet as the test case voxel size increased (0.938 and 1.25 mm), but were reduced in Unet-FT and Prognnet-FT. Prognnet reconstruction was less blurry than Unet. At voxel size = 0.577 mm, slight blurriness was observed in Unet and Prognnet but was reduced in Unet-FT and Prognnet-FT.

REFERENCES

1. Haacke EM, Xu Y, Cheng YCN, Reichenbach JR. Susceptibility weighted imaging (SWI). *Magnetic Resonance in Medicine: An Official Journal of the International Society for Magnetic Resonance in Medicine* 2004;52(3):612-618.
2. Haacke EM, Mittal S, Wu Z, Neelavalli J, Cheng Y-C. Susceptibility-weighted imaging: technical aspects and clinical applications, part 1. *American Journal of Neuroradiology* 2009;30(1):19-30.
3. Mittal S, Wu Z, Neelavalli J, Haacke EM. Susceptibility-weighted imaging: technical aspects and clinical applications, part 2. *American Journal of neuroradiology* 2009;30(2):232-252.
4. De Rochefort L, Liu T, Kressler B, et al. Quantitative susceptibility map reconstruction from MR phase data using bayesian regularization: validation and application to brain imaging. *Magnetic Resonance in Medicine: An Official Journal of the International Society for Magnetic Resonance in Medicine* 2010;63(1):194-206.
5. Kressler B, De Rochefort L, Liu T, Spincemaille P, Jiang Q, Wang Y. Nonlinear regularization for per voxel estimation of magnetic susceptibility distributions from MRI field maps. *IEEE transactions on medical imaging* 2009;29(2):273-281.
6. Liu T, Wisnieff C, Lou M, Chen W, Spincemaille P, Wang Y. Nonlinear formulation of the magnetic field to source relationship for robust quantitative susceptibility mapping. *Magnetic resonance in medicine* 2013;69(2):467-476.
7. Liu T, Khalidov I, de Rochefort L, et al. A novel background field removal method for MRI using projection onto dipole fields. *NMR in Biomedicine* 2011;24(9):1129-1136.
8. Schweser F, Deistung A, Lehr BW, Reichenbach JR. Quantitative imaging of intrinsic magnetic tissue properties using MRI signal phase: an approach to in vivo brain iron metabolism? *Neuroimage* 2011;54(4):2789-2807.
9. Fang J, Bao L, Li X, van Zijl PCM, Chen Z. Background field removal using a region adaptive kernel for quantitative susceptibility mapping of human brain. *J Magn Reson* 2017;281:130-140.
10. Sun H, Wilman AH. Background field removal using spherical mean value filtering and Tikhonov regularization. *Magn Reson Med* 2014;71(3):1151-1157.
11. Liu T, Liu J, De Rochefort L, et al. Morphology enabled dipole inversion (MEDI) from a single-angle acquisition: comparison with COSMOS in human brain imaging. *Magnetic resonance in medicine* 2011;66(3):777-783.
12. Shmueli K, de Zwart JA, van Gelderen P, Li TQ, Dodd SJ, Duyn JH. Magnetic susceptibility mapping of brain tissue in vivo using MRI phase data. *Magn Reson Med* 2009;62(6):1510-1522.
13. Wharton S, Bowtell R. Whole-brain susceptibility mapping at high field: A comparison of multiple- and single-orientation methods. *Neuroimage* 2010;53(2):515-525.
14. Wharton S, Schafer A, Bowtell R. Susceptibility mapping in the human brain using threshold-based k-space division. *Magn Reson Med* 2010;63(5):1292-1304.

15. Lu Z, Li J, Wang C, et al. S2Q-Net: Mining the High-Pass Filtered Phase Data in Susceptibility Weighted Imaging for Quantitative Susceptibility Mapping. *IEEE Journal of Biomedical and Health Informatics* 2022.
16. Kames C, Doucette J, Birkl C, Rauscher A. Recovering SWI-filtered phase data using deep learning. *Magnetic Resonance in Medicine* 2022;87(2):948-959.
17. Beliveau V, Birkl C, Stefani A, Gizewski ER, Scherfler C. HFP-QSMGAN: QSM from homodyne-filtered phase images. *Magnetic Resonance in Medicine* 2022.
18. Çiçek Ö, Abdulkadir A, Lienkamp SS, Brox T, Ronneberger O. 3D U-Net: learning dense volumetric segmentation from sparse annotation. *International conference on medical image computing and computer-assisted intervention*: Springer; 2016. p. 424-432.
19. Ronneberger O, Fischer P, Brox T. U-net: Convolutional networks for biomedical image segmentation. *International Conference on Medical image computing and computer-assisted intervention*: Springer; 2015. p. 234-241.
20. Zhang J, Zhang H, Spincemaille P, Nguyen T, Sabuncu MR, Wang Y. Hybrid optimization between iterative and network fine-tuning reconstructions for fast quantitative susceptibility mapping. *Medical Imaging with Deep Learning*: PMLR; 2021. p. 870-880.
21. Zhang J, Liu Z, Zhang S, et al. Fidelity imposed network edit (FINE) for solving ill-posed image reconstruction. *Neuroimage* 2020;211:116579.
22. Ren D, Zuo W, Hu Q, Zhu P, Meng D. Progressive image deraining networks: A better and simpler baseline. *Proceedings of the IEEE/CVF conference on computer vision and pattern recognition*; 2019. p. 3937-3946.
23. Kingma DP, Ba J. Adam: A method for stochastic optimization. *arXiv preprint arXiv:1412.6980* 2014.
24. Ioffe S, Szegedy C. Batch normalization: Accelerating deep network training by reducing internal covariate shift. *International conference on machine learning*: PMLR; 2015. p. 448-456.
25. Langkammer C, Schweser F, Shmueli K, et al. Quantitative susceptibility mapping: report from the 2016 reconstruction challenge. *Magnetic resonance in medicine* 2018;79(3):1661-1673.
26. Yoon J, Gong E, Chatnuntawech I, et al. Quantitative susceptibility mapping using deep neural network: QSMnet. *Neuroimage* 2018;179:199-206.
27. Bollmann S, Rasmussen KGB, Kristensen M, et al. DeepQSM-using deep learning to solve the dipole inversion for quantitative susceptibility mapping. *Neuroimage* 2019;195:373-383.
28. Zhang J, Zhang H, Sabuncu M, Spincemaille P, Nguyen T, Wang Y. Bayesian learning of probabilistic dipole inversion for quantitative susceptibility mapping. *Medical Imaging with Deep Learning*: PMLR; 2020. p. 892-902.
29. Zhang J, Zhang H, Sabuncu M, Spincemaille P, Nguyen T, Wang Y. Probabilistic dipole inversion for adaptive quantitative susceptibility mapping. *arXiv preprint arXiv:2009.04251* 2020.

30. Zhang H, Zhang J, Wang R, et al. Efficient folded attention for medical image reconstruction and segmentation. Proceedings of the AAAI Conference on Artificial Intelligence. Volume 35; 2021. p. 10868-10876.
31. Zhang J, Zhang H, Li C, et al. Temporal feature fusion with sampling pattern optimization for multi-echo gradient echo acquisition and image reconstruction. Medical Image Computing and Computer Assisted Intervention–MICCAI 2021: 24th International Conference, Strasbourg, France, September 27–October 1, 2021, Proceedings, Part VI 24: Springer; 2021. p. 232-242.
32. Jafari R, Spincemaille P, Zhang J, et al. Deep neural network for water/fat separation: supervised training, unsupervised training, and no training. Magnetic resonance in medicine 2021;85(4):2263-2277.
33. Gao Y, Cloos M, Liu F, Crozier S, Pike GB, Sun H. Accelerating quantitative susceptibility and R2* mapping using incoherent undersampling and deep neural network reconstruction. NeuroImage 2021;240:118404.
34. Zhang J, Spincemaille P, Zhang H, et al. LARO: Learned Acquisition and Reconstruction Optimization to accelerate Quantitative Susceptibility Mapping. NeuroImage 2023:119886.
35. Lai K-W, Aggarwal M, van Zijl P, Li X, Sulam J. Learned proximal networks for quantitative susceptibility mapping. Medical Image Computing and Computer Assisted Intervention–MICCAI 2020: 23rd International Conference, Lima, Peru, October 4–8, 2020, Proceedings, Part II 23: Springer; 2020. p. 125-135.
36. Polak D, Chatnuntawech I, Yoon J, et al. Nonlinear dipole inversion (NDI) enables robust quantitative susceptibility mapping (QSM). NMR in Biomedicine 2020;33(12):e4271.
37. Feng R, Zhao J, Wang H, et al. MoDL-QSM: Model-based deep learning for quantitative susceptibility mapping. NeuroImage 2021;240:118376.
38. Monga V, Li Y, Eldar YC. Algorithm unrolling: Interpretable, efficient deep learning for signal and image processing. IEEE Signal Processing Magazine 2021;38(2):18-44.